RESEARCH ARTICLE

ADVANCED
INTELLIGENT
SYSTEMS
Open Access

www.advintellsyst.com

Check for updates

Multistable Physical Neural Networks

Ben-Haim Eran, Givli Sefi, Or Yizhar, and Gat D. Amir*

Artificial neural networks (ANNs), which are inspired by the brain, are a central pillar in the ongoing breakthrough in artificial intelligence. In recent years, researchers have examined mechanical implementations of ANNs, denoted as physical neural networks (PNNs). PNNs offer the opportunity to view common materials and physical phenomena as networks, and to associate computational power with them. In this work, mechanical bistability is incorporated into PNNs, enabling memory and a direct link between computation and physical action. To achieve this, an interconnected network of bistable liquid-filled chambers is considered. All possible equilibrium configurations or steady-states are first mapped, and then their stability is examined. Building on these maps, both global and local algorithms for training multistable PNNs are implemented. These algorithms enable to systematically examine the network's capability to achieve stable output states and thus the network's ability to perform computational tasks. By incorporating PNNs and multistability, it is possible to design structures that mechanically perform tasks typically associated with electronic neural networks, while directly obtaining physical actuation. The insights gained from this study pave the way for the implementation of intelligent structures in smart tech, metamaterials, medical devices, soft robotics, and other fields.

1. Introduction

Brains are sophisticated biocomputational systems capable of performing multiple complex tasks simultaneously, yet are robust and remarkably power efficient.[1] Comprising billions of neurons interconnected by trillions of synapses, the human brain achieves these remarkable capabilities through extensive connectivity, a hierarchical functional organization, advanced learning rules, and neuronal plasticity.

Artificial neural networks (ANNs) were developed in order to enable bio-inspired learning capabilities. ANNs, however, are often computed using standard computers and lack many of the advantages of brain computation properties, such as parallelism, low energy consumption, fault tolerance, and inherent

B.-H. Eran, G. Sefi, O. Yizhar, G. D. Amir
Faculty of Mechanical Engineering
Technion–Israel Institute of Technology
Haifa 32000, Israel
E-mail: amirgat@technion.ac.il

robustness.[2] This led to the development of neuromorphic computing, a field that mimics the brain's computation process using physical mechanisms. The use of spiking neural networks on neuromorphic computing platforms, grounded in neural processing principles, provides researchers with valuable insights for constructing adaptive and efficient artificial intelligence (AI) systems.[3,4] This approach, influenced by advancements in materials engineering, device physics, chip integration, and neuroscience, has generated significant interest from both neuroscientists and computer scientists.

Comprehensive reviews, published in recent years, explored various facets of neuromorphic computing, covering device physics,[5–7] circuit design,[8,9] and network integration.[10,11] Training of neuromorphic systems, associated with physical learning, requires the modification of physical elements to provide desired computational outcomes. Previous studies involved training both simulated and laboratory mechanical networks, along with simulated flow networks, to perform specific tasks by adjusting their internal degrees of freedom.[12–24] This training is achieved through the minimization of a global cost function[17–21,25] or the application of local rules facilitated by an external processor.[12,14–16,22–24]

Mechanical,[17,24] flow,[24,26] and resistor networks[27] can perform tasks by transforming data into physical stimuli and responses, aligning with the common applications of machine learning. Moreover, these systems, devoid of memory storage, exhibit high robustness to damage, suggesting a novel direction for computer design. The interplay between learning and memory in physical systems underscores the importance of understanding properties contributing to memory retention, paving the way for leveraging material memory capabilities in training applications.[13,28,29] Bistable systems provide memory, programmability, and compact design, making them suitable for diverse applications, including wearable robotics and medical devices.[30,31] Moreover, metamaterials such as mechanical neural networks are being explored as potential solutions for precise control in soft robotics involving bistable elements. Bistability streamlines control complexities, offering energy-efficient and adaptable solutions for reliable soft robotic systems.[32–35] The dual-stable nature of bistable soft actuators conserves energy in static positions and enhances adaptability for variable stiffness and shape changes.[36]

In this research, *we aim to incorporate mechanical bistability into a physical neural network (PNNs), enabling memory and a direct link between computation and physical action.*

**ADVANCED
SCIENCE NEWS**

www.advancedsciencenews.com

**ADVANCED
INTELLIGENT
SYSTEMS**
Open Access

www.advintellsyst.com

The physical neural network examined in this work is constructed from a flow network characterized by bistable nodes, which incorporate internal, external, and output nodes. The objectives of this study are: firstly, to delineate the potential equilibrium configurations or the steady-states achievable by the network, including an in-depth examination of their stability; and finally, to train the network to perform desired tasks. A core challenge in training is determining a network topology and resistance configuration that directs the system to a desired equilibrium state within the range of possible states, under external loads. To address this, we developed two tailored methodologies: global and local supervised learning approaches. These methodologies leverage the network's mechanical properties to guide it toward achieving targeted goals.

2. Results

This study aims to combine multistability into physical neural networks. There are various possible physical systems, and in this study, we focus on a physical network consisting of N interconnected hyperelastic chambers (being the nodes) linked by rigid tubes (see **Figure 1**).

To explore the flow dynamics within the network, we formulate the system equations in matrix form. The pressures vector is represented as $\mathbf{p}(t) = [p_1, \ldots, p_N]^T$, where $p_i(t)$ is the hydrostatic pressure inside the ith chamber.[37,38] The nodes are modeled as elastic bodies (i.e., chambers) which can undergo volume changes, denoted by $\mathbf{v}(t) = [v_1, \ldots, v_N]^T$. The external volumetric flow is expressed as $\mathbf{q}(t) = [q_1, \ldots, q_N]^T$, where q_i represents a prescribed external volumetric flow into the ith node. Several assumptions are made to model the fluid behavior within this network: the fluid dynamic viscosity, μ, is constant, and the flow is laminar, fully developed, incompressible, and predominantly influenced by viscous forces. Furthermore, it is assumed that the viscous resistance of the nodes is negligible compared to that of the tubes. These conditions allow the use of the Hagen–Poiseuille law,[39] which characterizes the laminar flow of a Newtonian fluid through cylindrical tubes. Under these assumptions, the volumetric flow rates, Q_{ij}, between the ith and j^{th} chambers, governed by $Q_{ij} = C_{ij}(p_j - p_i)$, exhibit a linear dependence on their conductances, C_{ij}, where $C_{ij} = 1/R_{ij}$ and $R_{ij} = 8\mu\ell_{ij}/\pi a_{ij}^4$ represents the viscous resistance of the tube. This dependency is influenced by the tube's length, ℓ_{ij}, and is inversely proportional to the fourth power of the tube radius, a_{ij}.

Mass conservation at each node, while considering the entire network's conductances, yields

$$\frac{d\mathbf{v}}{dt} = -\mathbf{W}\mathbf{p} + \mathbf{q} \tag{1}$$

which is equivalent to Kirchhoff's law for the current system. The expression $W_{ij} = -C_{ij} + \delta_{ij}\sum_k C_{ik}$ represents the (weighted) graph Laplacian matrix, where δ_{ij} denoted Kronecher delta. It takes into account not only the network's connection topology but also the tubes' viscous resistance. The matrix $\mathbf{W}$ is singular, with all non-zero eigenvalues having a positive real part. We assume that the physical network can be represented as a connected graph, and that $\mathbf{W}$ is irreducible and its rank is $N-1$, with the smallest eigenvalue being zero and all others positive. Comprehensive mathematical details, including theorems and supplementary proofs, can be explored in classical literature on graph theory, such as reference.[40] The N nodes of the network include three subsets: b external inlet nodes

Single bistable node

Illustration of a fluidic bistable PNN
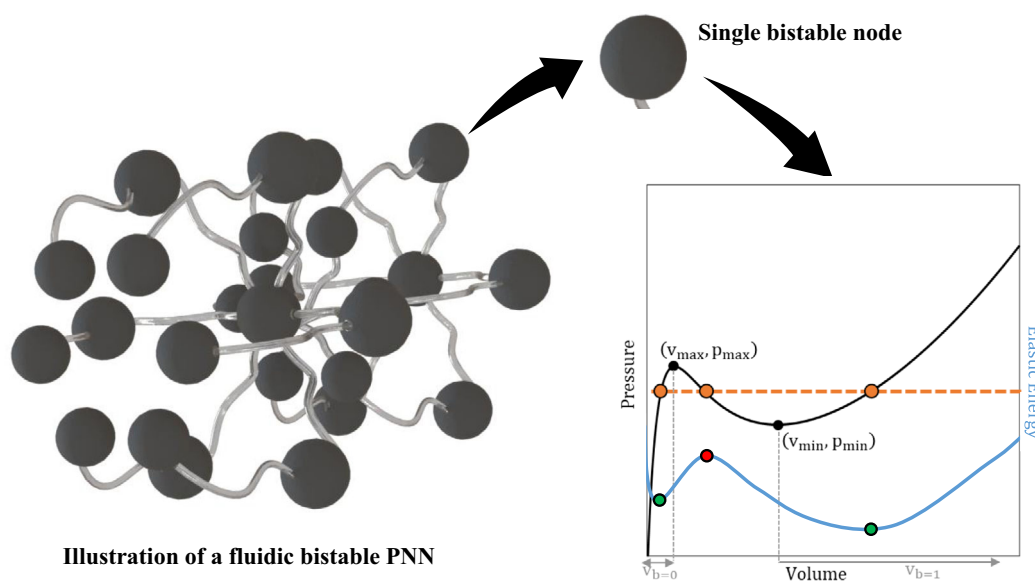
Figure 1. Illustration of a hierarchical metamaterial structure composed of bistable nodes interconnected by rigid tubes, showcasing the concept of design of the physical neural network in advanced metamaterial framework. Each node within this network is characterized by a distinct non-monotonic pressure–volume relationship, leading to two practical and stable equilibrium phases, symbolized as $v_{b=0}$ and $v_{b=1}$, or more simply, "0" and "1". Illustrated by the blue curve is the node's elastic potential, which clearly delineates two stable states separated by an unstable state, associated with the spinodal branch.

(denoted by $\mathcal{B}_0$) that serve as boundary conditions, t output nodes (denoted by $\mathcal{T}_0$) that serve as target nodes. The remaining d internal nodes are referred to as "hidden" nodes (denoted by $\mathcal{D}_0$). We note that $d + b + t = N$ holds. In addition, we divide the external nodes into two distinct types of boundary conditions: pressure-constrained external nodes and volumetric-constrained external nodes.

2.1. Bistable Network

2.1.1. Characterization of Pressure–Volume Relationship in Chambers

This work focuses on a physical bistable neural network. A *bistable* element is characterized by two distinct stable equilibrium configurations under the same prescribed load, separated by an unstable (spinodal) equilibrium state. Each bistable element is defined by a non-monotonic pressure-volume relation, $p_i = f(v_i)$, featuring two phases of positive stiffness, separated by an intermediate branch characterized by negative stiffness, as illustrated in Figure 1 in the pressure-volume characterization.[34,37,38,41–43] We note that the pressure-volume curve starts at zero pressure when no tensile forces are acting on the elastic wall, as in the case when gauge pressure is used. This zero-pressure point corresponds to a stress-free elastic configuration, where the chamber maintains an initial, non-zero volume.[34]

Next, we define a functional relationship between node pressure and volume, expressed as $\mathbf{p} = \nabla_{\mathbf{v}}^T \psi$, where ψ represents the total elastic energy, given by $\psi(\mathbf{v}) = \psi_1(v_1) + \ldots + \psi_N(v_N)$. This functional relation is applicable in situations where a (quasi-)static equilibrium is maintained, with the internal pressure of the body balanced by structural forces that counteract the pressure. Several examples of the use of such relations can be found in.[38,44]

For convenience, it is assumed that all elastic bodies have the same pressure-volume relation. Consequently, two distinctly separated equilibrium phases are denoted as "0" and "1" associated with volumes $v \in v_{b=0}$ for the "0" binary state, or $v \in v_{b=1}$ for the "1" binary state. The local minimum and maximum points of the pressure-volume relation are denoted as $(v_{\min}, p_{\min})$ and $(v_{\max}, p_{\max})$, respectively. Such behavior is observable in various structures such as curved beams,[45–50] thin-walled hyper-elastic balloons,[34,41–43] and pre-stressed elastic sheets.[51–54]

2.1.2. Network Equilibrium and Steady-States

Equilibrium in the system is achieved in the absence of external loading. A steady-state, on the contrary, is established when certain nodes are constrained to maintain a constant pressure and/or a constant flow, ensuring that the total incoming and outgoing flow at these nodes is balanced. In both cases, the total volume is conserved, necessitating that all nodes' pressures remain constant.

We define the initial volume of fluid within the network by v_0, which includes the chambers and tubes. To assess the total volume of the flow as a function of time, we consider the set of all nodes as a control volume, that is,

$$\mathbb{V}(t) = v_0 + \int_0^t \mathbf{1}_N \cdot \mathbf{q}(\tau)\mathrm{d}\tau \tag{2}$$

where $\mathbf{1}_N$ denotes the N vector of all unit elements. Steady-states of the system, where the total volume is conserved as $\mathbb{V}_{ss} = \lim_{t\to\infty}\mathbb{V}(t)$, necessitate that all nodes' pressures remain constant, namely, $\mathbf{W}\mathbf{p}_{ss} = \mathbf{q}_{ss}$, where $\mathbf{q}_{ss}$ denoted the flux injections vector where $t \gg 1$.

In cases where the external nodes are solely influenced by a prescribed flow rate (i.e., no external pressure constraints are applied), the steady-state solution is given by

$$\mathbf{p}_{ss} = \alpha \cdot \mathbf{1}_N + \mathbf{W}^\dagger \mathbf{q}_{ss} \tag{3}$$

where $\alpha \in \mathbb{R}$. The first right-hand term corresponds to the homogeneous solution, signifying a scenario with no injections into the network and equal pressures along the network (i.e., equilibrium state). The second right-hand term represents the particular solution, where $\mathbf{W}^\dagger$ is the *Moore–Penrose* inverse of the Laplacian matrix.[55]

In scenarios where a subset of $1 \leq b_1 \leq b$ external nodes undergo pressure constraints, $\mathbf{p}_{\mathbf{BC}} \in \mathbb{R}^{b_1 \times 1}$, while the remaining $b_2 = b - b_1$ nodes are governed by known volumetric fluxes, $\mathbf{q}_{\mathbf{BC}} \in \mathbb{R}^{b_2 \times 1}$; the system converges on a unique solution set that satisfies the boundary conditions, which is given by

$$\bar{\mathbf{p}}_{ss} = \mathbf{A}(\mathbf{W})\mathbf{p}_{\mathbf{BC}} + \mathbf{B}(\mathbf{W})\mathbf{q}_{\mathbf{BC}} \tag{4}$$

where $\bar{\mathbf{p}}_{ss}$ is the steady-state solution for the unloaded nodes, and $\mathbf{A} \in \mathbb{R}^{(N-b) \times b_2}$ and $\mathbf{B} \in \mathbb{R}^{(N-b) \times b_1}$ are two known matrices that depend on $\mathbf{W}$ and explicitly given in Equation (S3) and (S4) in Supporting Information.

We thus observe that, in the absence of external loading (i.e., a closed system without flux or prescribed pressure), the system displays uniform pressure across all nodes upon reaching an equilibrium state. Conversely, in scenarios where the system is subjected to external loads (be it through flux, pressure, or a combination) the resultant pressures at the nodes, post-convergence (i.e., in steady-state), are constituted by a linear combination of the system's constraints. This linear combination is significantly influenced by the elements of the Laplacian matrix, indicative of the system's dependence on both the network topology and the viscous resistances of the tubes.

Moreover, the relationship between pressure and volume at the nodes is crucial for understanding the system's dynamics, as it directly impacts flow rates, system capacity, and operational efficiency. For linear relationship, the combination of the known total volume, $\mathbb{V}_{ss}$, with the solution provided in Equation (3) or (4) yields a single solution, delineated by the steady-state configuration of the network. However, in the context of nonlinear nodes (i.e., nonlinear relationships between pressure and volume), such as multistable bodies, the aforementioned conditions may yield multiple solutions for node volumes. Since bistable relationships are not inherently reversible, the system's state is not uniformly defined in certain scenarios, so to extract volumes from pressure information, it is necessary to model the states of bistable chambers.

2.1.3. Network Stability

In what follows, we analyze the stability of the equilibrium and steady-states of the network. A comprehensive stability analysis is provided in Supporting Information. Here, we present only the main results to provide a complete overview.

The elastic network is governed by a scalar elastic energy function, $\psi_i(v_i)$, and the total elastic energy of the nodes is $\psi(\mathbf{v}) = \psi_1(v_1) + \ldots + \psi_N(v_N)$. Further, the total volume of flow within the network is known; hence, it is not necessary to solve all N equations of motion (for more details, see Section B in the Supporting Information). The resolution of $N-1$ equations is sufficient, achieved by removing one node arbitrarily. Returning to the general dynamic Equation (1), we omit the Nth degree of freedom, excluding the Nth row and column from the Laplacian matrix, along with the Nth element in the vectors $\mathbf{q}$, $\mathbf{p}$, and $\mathbf{v}$. The reduced system can be expressed as $d\tilde{\mathbf{v}}/dt = -\tilde{\mathbf{W}}\tilde{\mathbf{p}} + \tilde{\mathbf{q}}$. The constrained elastic energy function can be eliminated as $\tilde{\psi}(\tilde{\mathbf{v}}) = \psi(\tilde{\mathbf{v}}, v_N(\tilde{\mathbf{v}}))$ where $\tilde{\mathbf{v}} = [v_1, \ldots, v_{N-1}]^T$ is the reduced state vector, and $v_N(\tilde{\mathbf{v}}) = \mathbb{V} - (v_1 + \ldots + v_{N-1})$.

Examining the eigenvalues of the Hessian matrix of the (constrained) elastic energy, $\mathbb{H}_{\tilde{\mathbf{v}}}(\tilde{\psi})$, allows us to infer the stability of the network's states. An equilibrium state is stable if and only if the Hessian is positive definite, that is, $\mathbb{H}_{\tilde{\mathbf{v}}}(\tilde{\psi}) \succ 0$, which occurs if and only if all leading principal minors are positive, namely

$$\mathbb{M}_\gamma = \left[\prod_{i=1}^{\gamma} \frac{df_i}{dv_i} \right] \left[1 + \frac{df_N}{dv_N} \sum_{i=1}^{\gamma} \left(\frac{df_i}{dv_i} \right)^{-1} \right] > 0,$$
for all $\gamma \in [1, \ldots, N-1]$ (5)

As discussed in,[56] the equilibrium state of the network is based upon the distribution of nodes within the spinodal branch. A network devoid of nodes in the spinodal branch is in a state of stable equilibrium. Conversely, the existence of two or more nodes within the spinodal branch signifies an unstable equilibrium for the network. In the case where only a single node lies in the spinodal branch, the network achieves stability solely under the condition that

$$\sum_{i=1}^{N} \left(\frac{df_i}{dv_i} \right)^{-1} < 0$$ (6)

The study of the network's steady-states and the stability of its states reveals that in the absence of external loads, the network will attain a pressure equilibrium across any arbitrary topology. When the system is subjected to external loads, the steady-state pressures achieved are influenced by both the network's topology and the resistances of the tubes. While the existence of steady-state may rely on the topology and resistances, the steady-state stability of the network remains unaffected by these parameters. This finding catalyzes further investigation into bistable networks.

## 2.2. Resistance Tuning for Binary State Convergence in a Four-Node Network

In this section, we analyze a simple network consisting of four elements as a preliminary case study (see the inset in **Figure 2**), motivating the overarching goal of guiding flow networks toward a specific equilibrium state with known inputs. A pressure p_{BC} is prescribed to the inlet node; another non-adjacent node is grounded (i.e., zero pressure). The viscous resistances of the tubes are indicated by $R_{1,2,3,4}$, with R_1 and R_2 representing the resistances between the inlet node and the nodes number 1 and 2, respectively; and R_3 and R_4 representing the resistance between the nodes number 1 and 2 and the grounded node. At steady-state, according to Equation (4), the pressures of the two outlet nodes satisfy

$$p_1 = \frac{1}{1 + R_1/R_3} p_{BC}, \qquad p_2 = \frac{1}{1 + R_2/R_4} p_{BC}$$ (7)

It is observed that the nature of the steady-state, as described in Equation (7), is dictated by the ratios of viscous resistances, namely, R_1/R_3 and R_2/R_4. To illustrate the system's behavior, our analysis is delineated into two distinct scenarios—the first involves identical ratios. Subsequently, we explore the effects of different ratios.

In the scenario where the ratios satisfying $R_1/R_3 = R_2/R_4$, it is clearly apparent that steady-state is achieved when the pressures at the nodes equalize among themselves and $p_1 = p_2 = p_{BC}/2$. Considering this steady-state equation, when $p_{BC} > 2p_{\max}$ or $p_{BC} < 2p_{\min}$, a unique set of nodes' volumes is observed, as depicted in Figure 2a by dark-yellow points. This prescribed pressure leads to a stable binary configuration of (1,1) for the former case and (0,0) for the latter. Here, the binary state of node number 1 is denoted first, followed by the binary state of node number 2. However, the steady-state equation may describe multiple solutions for the nodes' volumes, if $2p_{\max} < p_{BC} < 2p_{\min}$. Under such conditions, each node may take one of three potential options, represented as orange points in Figure 2a. Consequently, we identify nine possible binary configurations, namely, (0,0), (0,s), (0,1), (1,0), (1,s), (1,1), (s,0), (s,s), and (s,1), where "s" represents the spinodal state. To examine the network's nature and the stability of resultant steady-states, especially under conditions presenting multiple steady-state possibilities, we direct the reader's attention to Figure 2b. This figure illustrates, within the state space $\{v_1; v_2\}$, the steady-state curves alongside the system's dynamic solutions under varying initial conditions. The solutions to the initial steady-state equation $p_1 = p_2$ are shown in the black curve, which includes a trivial line $v_1 = v_2$ and two additional curves forming a triangle-like feature for non-trivial solutions, where $v_1 \neq v_2$. Furthermore, the steady-state must also satisfy $p_{BC} = 2p_1$ and $p_{BC} = 2p_2$. These conditions are represented by three distinct lines within the $\{v_1; v_2\}$ space, each illustrating the three potential volumes for pressures that lie between the local minimum and maximum pressure points in pressure-volume characteristic—$\hat{v}_{b0} \in v_{b=0}$ for volumes within the binary domain "0", $\hat{v}_{b1} \in v_{b=1}$ for the binary domain "1", and $\hat{v}_s \in v_s$ for the spinodal domain. Consequently, by intersecting all steady-state curves within this space, nine fixed points emerge. Points of stable configuration are highlighted in
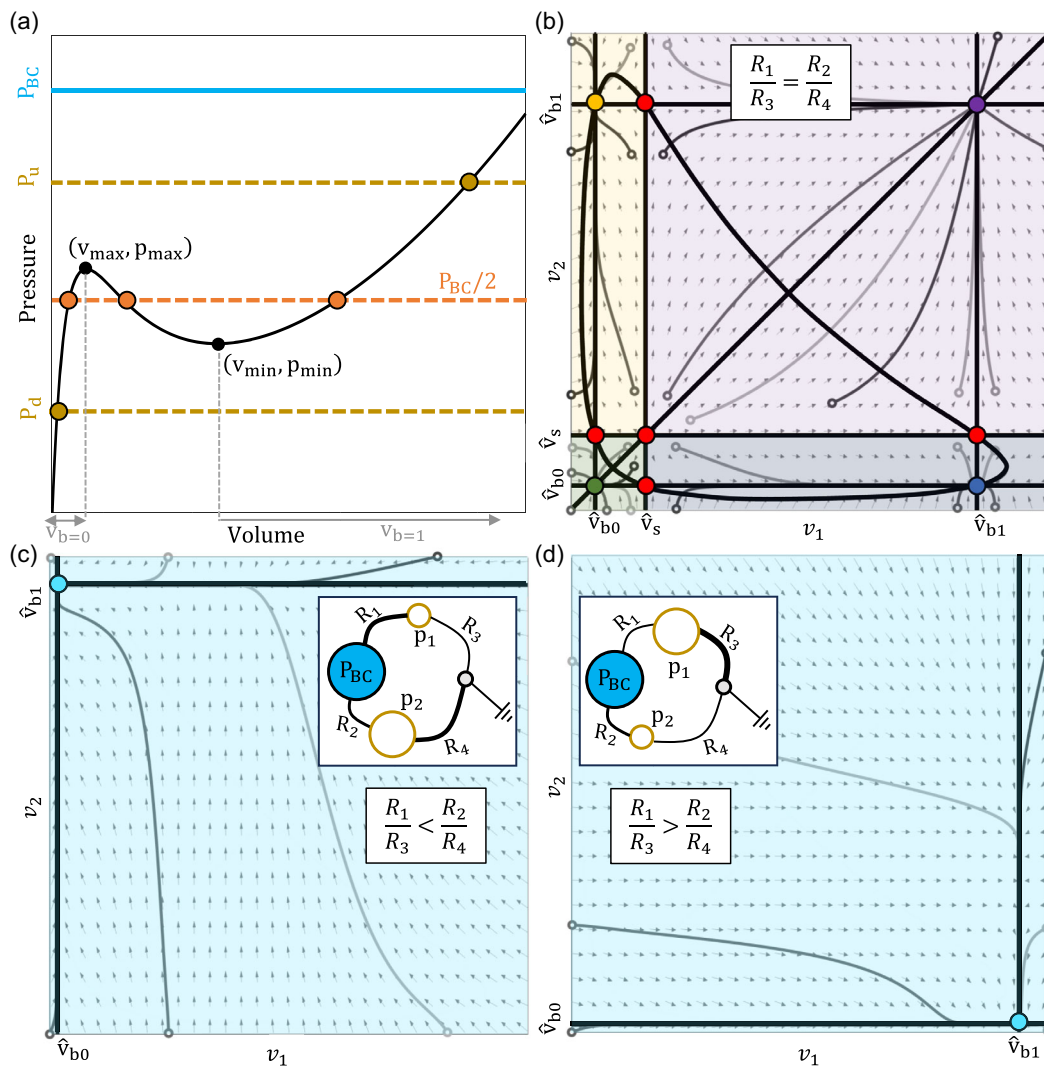
Figure 2. A theoretical investigation of a grounded flow network with four bistable nodes dictated by external pressure p_{BC}. The viscous resistances are denoted by $R_{1,2,3,4}$. a) Typical pressure–volume curve of a bistable element. The domain of volumes in binary states "0" and "1" is $v \in v_{b=0}$ and $v \in v_{b=1}$, respectively. A pressure higher than p_{max} or lower than p_{min} is denoted by p_u and p_d, respectively, and the volumes are defined in a one-value manner. For a pressure within the bistable domain, there are three different options for volume, marked by orange dots. b) $\{v_1; v_2\}$ space to describe the dynamic solutions of the system for the case where $R_1/R_3 = R_2/R_4$. The black lines are solutions of the steady-state equations. The intersection between these lines describes the fixed points of the system (green, blue, orange, and purple are stable, red is unstable). The gray arrows describe the dynamic solution field, namely, $\{v_1(t), v_2(t)\}$. Several solution trajectories (gray curves) are presented for different initial conditions (marked with empty circles). The colored regions indicate the areas where initial conditions will eventually converge to their corresponding stable equilibrium points, represented by the same colors. c) $\{v_1; v_2\}$ space to describe the network dynamics for the case where $R_1/R_3 < R_2/R_4$. In the described map, there is one fixed point described by the stable binary state (0,1) to which the network reaches from any initial conditions. d) $\{v_1; v_2\}$ space to describe the network dynamics for the case where $R_1/R_3 > R_2/R_4$. In the described map, there is one fixed point described by the stable binary state (1,0) to which the network reaches from any initial conditions.

green, blue, orange, and purple, whereas unstable configuration points are denoted in red. The stability of these points is determined based on the analysis Section 2.1.3. Following our stability analysis, the system converges to different equilibrium points based on the initial conditions, $\{v_{1,0}, v_{2,0}\}$. Specifically, for initial conditions where $v_{1,0} < \hat{v}_s$ and $v_{2,0} < \hat{v}_s$, the system converges to the green equilibrium point, while conditions where $v_{1,0} > \hat{v}_s$ and $v_{2,0} < \hat{v}_s$ lead to the blue equilibrium point. Similarly, when $v_{1,0} < \hat{v}_s$ and $v_{2,0} > \hat{v}_s$, the system converges to the equilibrium

point marked in orange, and for $v_{1,0} > \hat{v}_s$ and $v_{2,0} > \hat{v}_s$, it converges to the purple equilibrium point. These regions are highlighted in the background of the panel.

In the scenario where $R_1/R_3 \neq R_2/R_4$, the equilibrium pressures between the two nodes diverge, breaking the symmetry between the network's branches. Through a strategic choice of resistance ratios, the network can achieve two stable but opposite binary states under the same applied pressure. For illustrative purposes, we assume at steady-state one node stabilizes at a

**ADVANCED
SCIENCE NEWS**

www.advancedsciencenews.com

**ADVANCED
INTELLIGENT
SYSTEMS**
Open Access

www.advintellsyst.com

pressure above p_{max} (denoted as p_u, illustrated in Figure 2a), while the pressure at the other node is below p_{min}, represented as p_d. This configuration yields a single steady-state, contingent upon the resistance ratios. If $R_1/R_3 > R_2/R_4$, it follows that $p_1 = p_u$ and $p_2 = p_d$, guiding the network to a stable steady-state in the (1,0) binary configuration from any initial condition. Conversely, if $R_1/R_3 < R_2/R_4$, then $p_1 = p_d$ and $p_2 = p_u$, resulting in a stable steady-state in the (0,1) binary configuration from any initial state. These outcomes are displayed in Figure 2c,d. It is relevant to note that the removal of the assumption regarding the nodes' pressures relative to p_{max} and p_{min} introduces additional stable binary states, such as (0,0) or (1,1). In this case, the system's convergence toward a specific state becomes dependent on the initial conditions, further enriching the dynamical behavior.

From the above, it is evident that both the network topology as well as the tube resistances have a significant influence on the network's steady-state, specifically regarding the binary state configuration, in terms of convergence of flow. While the topology does not alter the stability of the steady-states, it impacts the existence of these points and the network's convergence basins toward equilibrium. Given a predetermined input, planning of topologies can steer networks toward specified steady-states. However, the scenario analyzed here represents a basic and degenerate scenario. The structure of networks with more interconnections and complexity, on the contrary, requires more advanced methods. This study will elaborate on these methods in subsequent sections.

2.3. Network Morphology and Topological Study

In earlier studies, flow networks underwent training to demonstrate the specific function of flow allostery[19,21] through global supervised learning, involving the minimization of a global cost function. This training was primarily focused on ensuring the networks could exhibit a desired pressure drop across a target edge (or multiple target edges) when a pressure drop is applied across a source edge. However, as discussed earlier, relying solely on the desired pressure drop across a target edge is insufficient for defining the equilibrium state of bistable networks, as it neglects the consideration of binary states.

In the following sections, we introduce two distinct training methodologies designed for the analysis of bistable flow networks, each tailored to meet specific network requirements and external loading conditions. These complementary approaches are presented to achieve the overarching goal of training the network topology and resistances to reach a desired equilibrium state. Each method offers unique advantages and limitations that will be discussed further in this work.

Initially, we explore a scenario where the network operates without external pressure loading, functioning as a closed physical system. Within this framework, the system is capable of adopting 2^N different binary configurations, with the resulting configuration of convergence being influenced by both the total volumetric flow within the network and its topology. We postulate an initial state wherein the nodes are devoid of gauge pressure; subsequently, a volumetric flux is introduced into the network through specific nodes over a predetermined duration.

The primary challenge lies in identifying topology and a set of viscous resistances that drive the system toward a preferred equilibrium from the potential equilibrium configurations. To address this, we employ a *global supervised learning* approach, which will be discussed later.

In the subsequent analysis, our focus shifts to networks wherein the input nodes are subjected to prescribed boundary conditions pressures. There, the objective transitions to determining a resistance configuration that aligns the pressures and binary states at the output nodes with targeted values. This process is facilitated through the utilization of a *local supervised learning* method.

2.3.1. Training via Global Supervised Learning Approach

Here, we present a methodology for determining a flow network topology and resistance to perform multiple tasks using the same acquired structure. To this end, our approach involves optimizing a global cost function for bistable flow networks.

In this context, we aim to use a training algorithm in order to reach various equilibrium states based on different sets of sources (out of the 2^N possible states). More specifically, assuming a series of vectors $\{\mathbf{q}^{(h)}(t)\}_{h=1}^k$, for each vector $\mathbf{q}^{(h)}(t)$ the system is expected to converge to a (distinct) final state denoted by $\mathbf{v}_{ss}^{(h)}$. For each vector $\mathbf{q}^{(h)}(t)$, we establish a target volume vector $\mathbf{v}_t^{(h)}$. The primary goal is to identify a particular Laplacian matrix $\mathbf{W}$ (which represents the topology and the tubes' resistance) that guarantees the system's convergence to the state closest to the specified target state, for each task.

The volume state vector of the flow can be (implicitly) calculated through the time integration of the equation of motion (1), that is,

$$\mathbf{v}^{(h)}(t) = \mathbf{v}_0 + \int_0^t \mathbf{q}^{(h)}(\tau)d\tau - \mathbf{W}\int_0^t \mathbf{p}(\mathbf{v}^{(h)}(\tau))d\tau \tag{8}$$

Upon the system achieving a steady-state (or an equilibrium), the steady-state volume vector is calculated by $\mathbf{v}_{ss}^{(h)} = \lim_{t\to\infty} \mathbf{v}^{(h)}(t)$. We note that for any Laplacian matrix $\mathbf{W}$, the relation of the total volume (2) holds. This can be easily demonstrated by projecting the vector (8) onto $\mathbf{1}_N$ and utilizing the fact that the sum of the columns of $\mathbf{W}$ equals zero. The requirement for the hth target vector is that $\mathbb{V}_{ss}^{(h)} = \mathbf{1}_N \cdot \mathbf{v}_t^{(h)}$, ensuring compliance with the overall volume constraint. The *loss-function* is defined as the Euclidean norm of the volume state vector and the corresponding target vector in the steady-state, namely

$$\mathscr{L} = \frac{1}{k}\sum_{h=1}^k \|\mathbf{v}_{ss}^{(h)} - \mathbf{v}_t^{(h)}\|_2^2 \tag{9}$$

To determine a specific Laplacian matrix that ensures the system's convergence to the target state, we introduce the following optimization problem:

$$\underset{\mathbf{W}}{\text{minimize}} \quad \mathscr{L}(\mathbf{W}) + \beta\|\mathbf{W}\|_2^2$$
$$\text{subject to} \quad W_{ij} = W_{ji} \leq 0, \ i \neq j \tag{10}$$
$$\mathbf{W}\mathbf{1}_N = \mathbf{0}_N$$

where $\mathbf{0}_N$ denote the N-vector of all zeros entries and the positive scalars β is a regularization parameter. The constraints ensure that the trained Laplacian matrix ($\mathbf{W}$) is valid and positive semidefinite. A closed-form solution to the problem appears unattainable, primarily due to the non-convex nature of the problem and the absence of an explicit presentation of the dynamic solution. To address this, we have employed the *projected gradient descent* algorithm (PGD) for a numerical approach to solving the optimization problem.[57] For more details, the reader is encouraged to refer to Section C in the Supporting Information. Moreover, the minimization problem outlined in (10) is addressed in Section G in the Supporting Information by Algorithm 1. It should be noted that the existence of a solution is not guaranteed. Furthermore, even if a solution does exist, it is not necessarily unique.

The subsequent part showcases three numerical demonstrations of networks where the training algorithm has successfully converged. The elastic nodes are implemented as hyperelastic balloons, parameterized by the Ogden model,[58] which exhibit a bistable pressure-volume relation. Key learning parameters, including learning rate factor $\eta = 0.1$ (see Equation (S22) in Supporting Information) and $\beta = 10^{-5}$, were incorporated. The system underwent a controlled introduction of constant flux within specific time intervals to facilitate the attainment of equilibrium. In both simulations, a reasonable constraint was applied to limit the range of resistances in the model: tubes with a resistance exceeding 5 (Pa s mm^{-3}) were removed entirely, while the minimum allowable resistance was set at 0.2 (Pa s mm^{-3}). During the learning process, resistances exceeding five times the initial values were observed to behave similarly to models where the corresponding tube was removed. Thus, these tubes were omitted in order to simplify the network. On the contrary, in order to avoid excessively low resistance values and negative values, a lower threshold was established. While lower thresholds extended the iterative process due to closer dynamics between neighboring nodes, a threshold of one-fifth of the initial value was chosen, as it provided a balance between computational efficiency and result quality.

The first network contains a 5×5 lattice, consisting of 25 nodes (see **Figure 3**). This lattice was trained with a dual-task objective: a distinct set of outlet nodes experienced a binary state transition, resulting in the visual appearance of diagonal lines below the input node. Meanwhile, the binary states of the remaining internal nodes were set to "0". In the second task, when a single inlet node transitioned to binary state "1", a specific set of target nodes also underwent a binary state transition to "1", resulting in the formation of a visual rhombus around the inlet node. Once more, the internal nodes maintained a state of "0" (see Figure 3a). The second successfully trained network, also comprising a 5×5 lattice of nodes, identifies the left column as an input column. Each node in this column is assigned a specific input number, from 1 at the top to 5 at the bottom. By introducing an influx in the input column and transitioning one of the nodes to binary state "1", the network's task is to register the digit of the nodes where the flow is inserted. The process involves activating the corresponding nodes to the binary state "1" while keeping the other nodes in a state of "0" (see Figure 3b).

Further, each bistable node in the network can be viewed as a binary digit, allowing the entire multistable PNN to function as a memory storage device—a concept applicable to any multistable system. The primary challenge in such networks is to generate, store, access, and use information at specific locations within the network during computations. To address this, our algorithm employs two signals spaced apart by a duration longer than the network's stabilization time, ensuring that after the first signal, the network reaches a stable equilibrium state that serves as memory. Owing to the bistability property, following the initial signal, the nodes that become inflated remain so even after disconnection from external inputs. In this intermediate configuration, these nodes are fixed in binary state 1, while all other nodes reside in binary state 0. Despite this distinction, all nodes maintain a uniform pressure, consistent with the conditions of physical equilibrium. In **Figure 4** we demonstrate the results of this approach, by utilizing memory during computation for multistable PNNs that have been trained using the above-described global learning algorithm. Two nodes form the input layer of this network, which is followed by a 5×5 node lattice with two nodes forming the final layer of the network. Two identical PNNs are presented, highlighted with green and orange frames in Figure 4b,c. Each of the identical PNNs receives a different initial input flow signal. The inputs are identical in magnitude and duration, but directed to different nodes, specifically to numbers 1 and 2 in the input layer of each structure. As soon as the systems have stabilized and reached equilibrium, they are then disconnected from external loads, retaining the embedded memory of the initial input in column 4, (see Figure 4b). Following this step, both networks receive the same secondary input signal through node number 1, and are once again allowed to stabilize (Figure 4c). Within the lattice, the equilibrium state of the first network reveals a single column of nodes in the binary state "1", with all other nodes in the binary state "0". In contrast, the equilibrium state of the second network features two columns of nodes in the binary state "1", demonstrating that the network's response is affected by both the current, and previous inputs.

In Section F of the Supporting Information, we present a list of viscous resistances derived from the simulations shown in Figure 3 and 4.

2.3.2. Training via Local Supervised Learning Approach

Transport of materials in both biological networks, such as vascular systems, and engineered counterparts, like microfluidic networks, commonly rely on fluid flow. The pipes' properties, such as radii, conductance, and capacitance, collectively influence the network's global material transport capabilities, making it effective. Although computational optimization is a viable strategy, many natural systems tend to adjust individual elements based on localized feedback. In some instances, the flow within pipes can interact with the mechanical characteristics of these tubes, leading to localized adaptations such as constriction or expansion. These adaptations serve to regulate local flow conductance and pipe capacitance, providing the network with a mechanism to control cargo distribution. For example, in *Physarum polycephalum*, the thickness of tubes governs the organism's shape, enabling it to move, forage, and memorize features of its environment.[59–61] Similarly, adaptive processes in other natural flow networks, such as those in leaves and vasculature,[62,63]
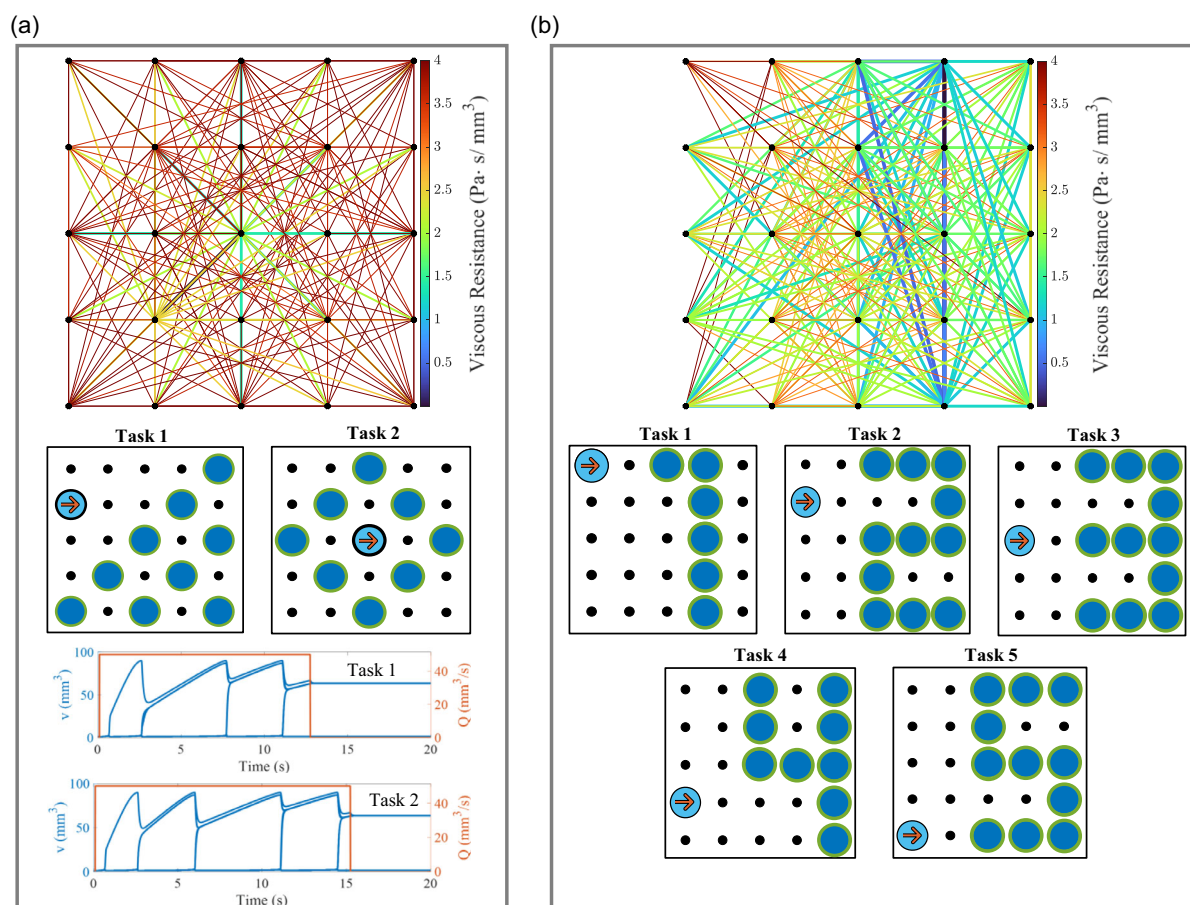
Figure 3. Illustration of two numerical simulations showcasing the learning capabilities of a metamaterial composed of a bistable flow network. The elastic nodes are considered to be bistable elements characterized by a distinct non-monotonic pressure–volume relationship as described in Figure 1, modeled as hyperelastic balloons, utilizing the Ogden model.[58] An initial volume of 1 cc indicates a stress-free elastic configuration (i.e., zero gauge pressure). These balloons incorporate a bistable regime (between 0.8 and 1.1 Pa), transitioning from binary state "0" to "1" at a volume of 2.55 cc and reverting from state "1" to "0" at 22 cc. Learning parameters included learning rate $\eta = 0.1$ and $\beta = 10^{-5}$. Steady-state convergence pressure was set at 0.9 Pa. A constant flux was introduced into the system during a specific period of time, allowing it to reach equilibrium. The initial viscous resistances were set to unity. a) Results for the first network, indicating the obtained connection topology, colored by viscous resistance and thickness. The middle section depicts the system results in equilibrium, highlighting the inlet and target balloons. The lower part shows volume changes over time (in blue) and the entering flow (in red), obtained by numerical integration of (1) using ode45 in Matlab. Those nodes that do not snap to the binary state "1" remain nearly at their initial volume, while others snap through in a sequence defined by the resistance configuration. Some snapped nodes exhibit so similar dynamic responses that their graphs appear virtually indistinguishable. b) Figure results for the second network, which mastered five tasks, visually displaying the digit representing the inserted flux's entry balloon in the input layer.

operate through local rules, without a centralized controller. Theoretical explorations of such flow networks have inquired into their potential to learn diverse behaviors through local rules, including classifying stimuli reminiscent of machine learning principles.[16,17,26,27]

Here, we focus on bistable networks with sustained pressure applied to their external nodes (as a boundary condition). These systems always reach a stable steady-state, requiring a period of relaxation. The main objective is to align the steady-state output nodes' binary states (and corresponding pressures) with the predefined targets. During the training, inputs and outputs are specified. To achieve these desired output pressures, the learning degrees of freedom of some tubes must be fine-tuned. The algorithm designed for instructing the system to attain the prescribed pressure has been described in the works of[17,27] for other

applications under the assumption that networks maintain linear relationships. Their algorithm is briefly described in Section D in the Supporting Information. In the context of a bistable network, however, it becomes imperative to modify the algorithm steps. In the following discussion, key adjustments to the algorithm are outlined.

Since the relation between pressure and node volume is complex, nonlinear, and bistable, our initial emphasis is on making sure each node's binary state aligns with the target binary state, representing the desired result. Subsequently, careful fine-tuning of the viscous resistances ensues to guide the nodes to the required pressure within the correct binary state. This algorithm hinges on the memory property inherent in bistable networks. The system converges to a stable steady-state at every stage. This stable state serves as the initial condition for the
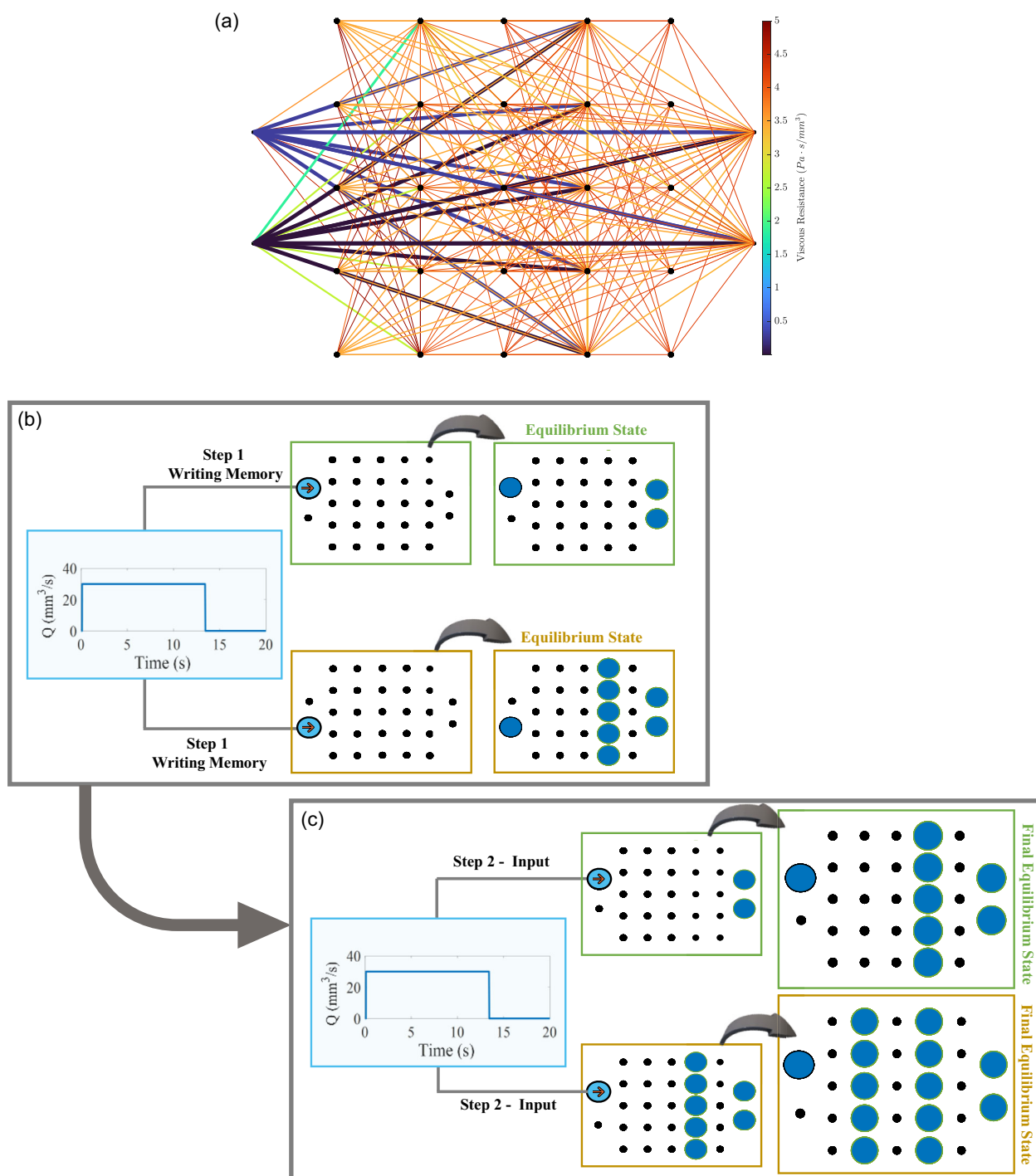
Figure 4. Demonstration of bistable PNNs memory. a) The input layer of this network is composed of two nodes. The next layer is composed of a 5 × 5 node lattice, with two nodes as the final layer. We examine two identical topology structures presented in (a), highlighted with green and orange frames in panels (b) and (c). b) Flow signals are directed to nodes 1 and 2 in each structure's input layer. Once both networks have reached equilibrium, c) both are given the same input signal through node number 1, and are allowed to stabilize again. There is one column of nodes in the binary state "1" within the lattice of the first network, and all other nodes are in the binary state "0". In contrast, the equilibrium state of the second network features two columns of nodes in the binary state "1", which indicates that the network's response can vary significantly depending on history and, therefore, the initial state.

**ADVANCED
SCIENCE NEWS**

www.advancedsciencenews.com

**ADVANCED
INTELLIGENT
SYSTEMS**
Open Access

www.advintellsyst.com

subsequent iteration of the learning. Through such a mechanism, the system can attain unique convergence basins that would not be possible without preserving intermediate states. The pseudo-code for our learning algorithm can be found in Algorithm 2 in Supporting Information.

Throughout the training regimen, changes to viscous resistances are executed through a comparative analysis of two distinct flux states imposed on the same network by different boundary conditions-denoted as free and clamped networks. In the free state, the network attempts to accomplish the designated task by applying input pressures, $\mathbf{p_{BC}}$, and subsequently producing corresponding output pressures, $\mathbf{p_{out}^f}$, and binary states for each output node. In the clamped state, identical inputs are applied, $\mathbf{p_{BC}}$, but additional pressures are applied at the output nodes. In this context, we distinguish two scenarios: when the binary state of the node is not acceptable (i.e., does not meet the target binary state), this node shall transition between the binary states. Specifically, when transitioning the node from binary state "0" to binary state "1", the dictated pressure exceeds the local maximum point in the pressure-volume characteristic. Conversely, when transitioning the node from the binary state "1" to "0", the dictated pressure is set below the local minimum point in the pressure-volume characteristic. In cases where the binary state of the output node is acceptable (i.e., meeting the target), the dictated pressure follows the[17,27] algorithm as described in Section D in the Supporting Information. Moreover, applying our local-learning algorithm involves numerically solving N nonlinear ODEs at each iteration. Networks with large sizes or high resistance may experience inefficient computations or convergence challenges. In Section E in the Supporting Information, we describe our alternative algorithm for optimizing the training methodology without repeating differential equation resolutions.

Below, we present three simulations showcasing the success of the learning process for bistable flow networks utilizing the aforementioned algorithm. Initially, we devised a disordered network of nodes, randomly located in the plane, stipulating that the minimum distance between adjacent nodes exceeds a predefined threshold. The nodes were interconnected by tubes, ensuring that each node was linked to up to the five closest nodes, under the condition that the distance did not surpass a predefined value. The (initial) viscous resistances of the network were defined proportionally to the distance between nodes. We began with an initial volume of 1 cc indicating a stress-free elastic configuration (i.e., zero gauge pressure). In **Figure 5**, we illustrate training outcomes for two networks comprising 150 nodes each and another network with 100 nodes. In each simulation, the input nodes were randomly designated (highlighted in blue), and output nodes were also randomly selected (highlighted in orange and yellow for two exit nodes, or yellow, orange, purple, and green for four exit nodes). In the presented simulations, we employed a theoretical bistable characteristic that correlates pressure to the volume of nodes, approximating a simple trilinear curve for simulation simplicity. This characteristic delineates two distinct binary states: state "0" for volumes smaller than 5 cc and state "1" for volumes greater than 9 cc (recall that the middle branch, the spinodal, is unstable and is denoted by a dashed line). The displayed error, labeled as *Error*, is defined by the squared norm difference between the volumes obtained

in the simulation and the volumes defined as the target. We examine the difference between volumes rather than pressures since the nodes are characterized by a trilinear curve, and tracking pressure does not uniquely describe the network's state.

In the initial simulation, presented in Figure 5a, a network comprising 150 nodes was defined. Two nodes were set to pressures of 0 and 8 Pa, with two specific goals outlined: one node aimed to achieve a pressure of 5 Pa and be in a binary state "1", while another node was to reach a pressure of 1 Pa and be in a binary state "0". The algorithms of[17,27] could be employed for training in this scenario; however, the enhanced algorithm we introduced significantly optimizes the learning process and reduces the number of iterations needed for convergence. In the initial iteration, the first output node (marked in yellow) converged to an incorrect binary state regarding the target. However, in the subsequent iteration, owing to our learning process, the node converged to the desired state. Consequently, the error is also discontinuously decreased, as expected during the "snap-through" transition of the system through an unstable branch. Figure 5a,b displays multiple panels, including pressure as a function of time representing the pressures of the output nodes. Other panels illustrate volume as a function of time, pressure as a function of volume, and the error as a function of iterations. Additionally, visualizations of the initial (untrained) network and the final trained network are presented. The colors of the tubes are mapped according to the scale of the viscous resistances corresponding to those tubes, and the thickness is proportional to the viscous resistance (i.e., greater resistance corresponds to smaller line thickness, and vice versa). Remarkably, the network demonstrated successful training after only 30 iterations in this simulation.
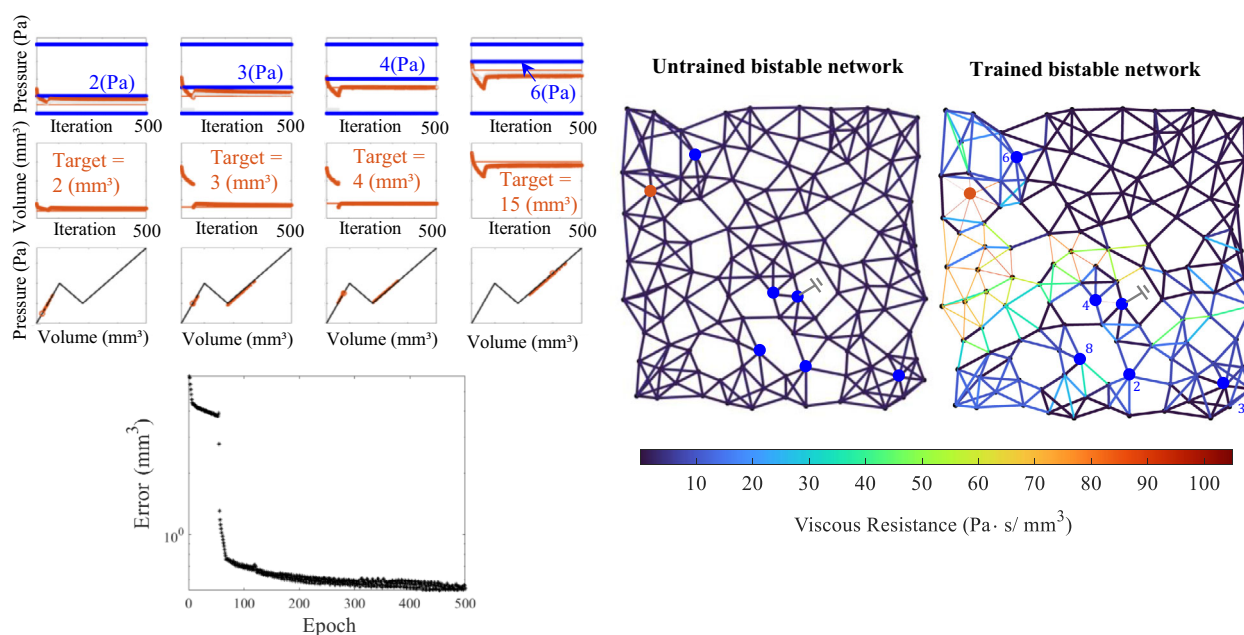
In the second simulation, we modified the target pressures to lie within the bistable region of the pressure-volume curve, setting them at 3 Pa. For one output node, we specified it to be in binary state "0", while for the second output node, it was set to be in binary state "1". Similar to the preceding simulation, the success of the learning algorithm is evident, with the network converging after only 128 iterations. Based on this simulation, the learning process presented in this paper has several strengths. Firstly, the capability of the first output node to reach the binary state "1" and reside within the bistable region is achieved exclusively through the system's memory feature. This highlights the indispensability of this feature for attaining the requisite state. Additionally, the algorithm successfully discriminates between the distinct binary states of the nodes, even when the target pressures are identical.

In the third simulation, we present the training results of a 100-node network tasked with achieving four goals. The objectives incorporate elements from the two prior experiments, requiring two output nodes to reach pressures of 1 and 5 Pa, and an additional two output nodes to attain identical pressures of 3 Pa but at different binary states. Furthermore, three input nodes were defined in this simulation with applied pressures of 7 and 8 Pa. In Figure 5c, we depict slightly different panels than before, showcasing pressure and volume as functions of the iteration number. Each point in the graph represents the pressure (or volume) to which the system has converged in a steady-state. Specifically, in the first iteration, the four outlet nodes reached pressures higher than required. Consequently,
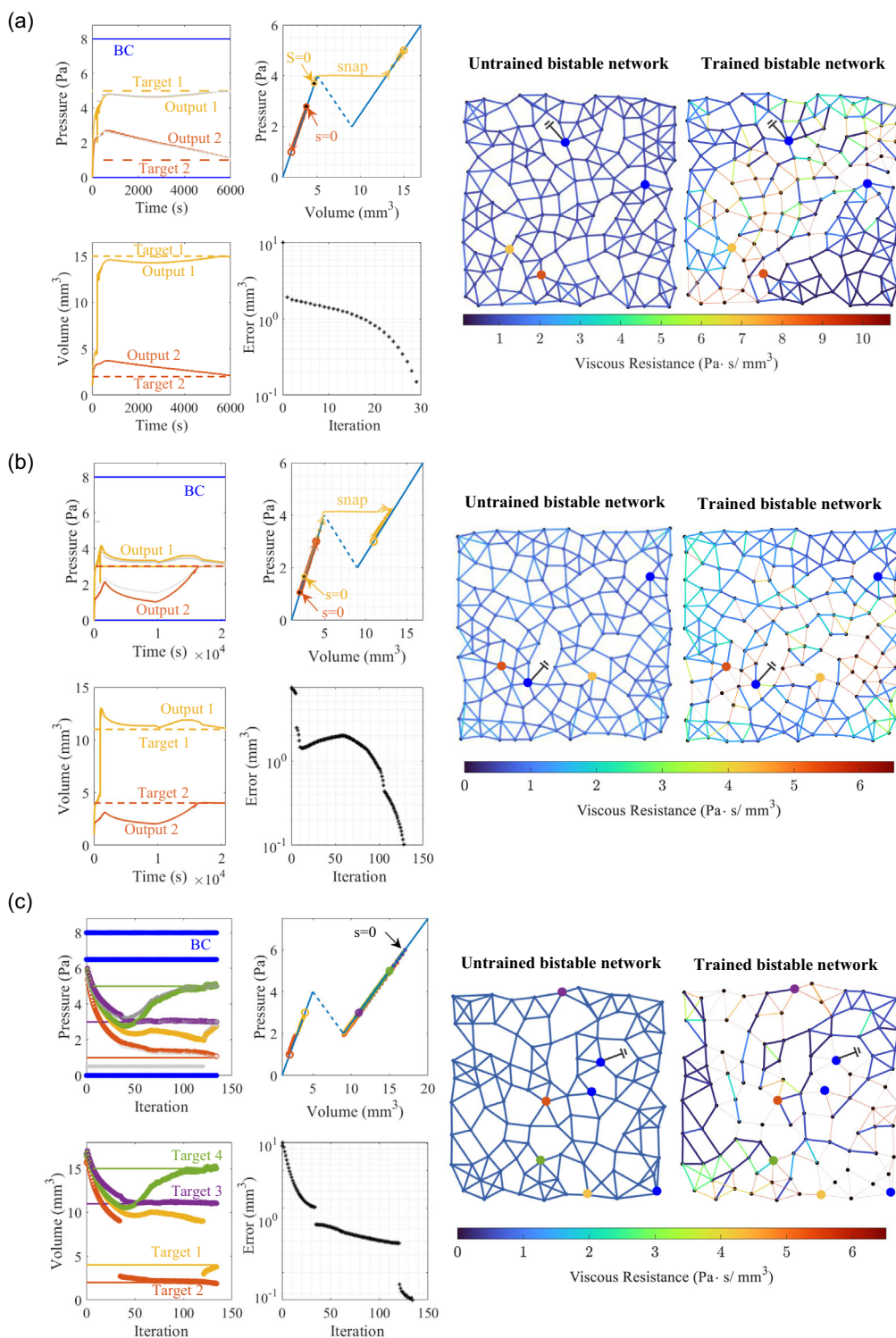
Figure 5. Illustration of three numerical simulations demonstrating the local-learning algorithm of a bistable flow network. For the simulation, we set the parameters $\eta = 0.25$, $\gamma = 0.01$, and defined the convergence when the error reaches 10^{-1}. Theoretical bistable characteristics, simplifying to a trilinear curve, were employed for simulation. The unstable spinodal is denoted by a dashed line. The *Error* indicates the squared norm difference between simulated and target volumes. The first learning iteration is indicated by the notation $s = 0$. a,b) Illustration of training outcomes for two 150-node networks, in which blue nodes represent input nodes, and orange/yellow output nodes aim to reach specified pressures and binary states. Gray lines represent supervisor pressure constraints. A series of panels shows the training process through pressure–time, volume–time, pressure–volume, and error iterations. Visualization includes initial and final networks, with tube colors and thickness indicating viscous resistance. c) Results of a 100-node network achieving four targets are presented, with each point representing the converged steady-state pressure or volume.

**ADVANCED
SCIENCE NEWS**

www.advancedsciencenews.com

**ADVANCED
INTELLIGENT
SYSTEMS**
Open Access

www.advintellsyst.com

Figure 6. Numerical simulation conducted on a grounded network with 150 nodes and five inputs, aimed at training the output node for multiple tasks with varying inputs. The elastic characteristic (pressure–volume relationship) of each node corresponds to the profile depicted in Figure 5. Parameters were set as $\eta = 0.25$, $\gamma = 0.01$, with convergence defined by an error threshold of 5×10^{-1}, where "Error" denotes the mean of squared norm difference between simulated and target volumes for each task. Constant inlet pressure was maintained at 8 Pa (and 0 Pa), while other inlets varied between 2, 3, 4, and 6 Pa, targeting output volumes of 2, 3, 4, and 15 cc^3, respectively. Blue nodes indicate inputs, with the orange output node reflecting the aim to achieve specified pressures and binary states. Both initial and final network states with variations in vortex colors and thickness illustrate changes in viscous resistances.

during the learning process, two abrupt transitions were executed to attain appropriate binary states (from "0" to "1"), demonstrated by the sharp jumps in the volume graph for output nodes 1 and 2 and the Error graph. This simulation also demonstrates excellent convergence of the learning algorithm, indicating success in training a bistable flow network to accomplish multiple tasks.

Finally, **Figure 6** showcases the outcomes of a simulation conducted on a grounded network comprising 150 nodes with five inputs. This simulation aims to train the output node to execute multiple tasks under varying inputs. Accordingly, one inlet pressure was maintained constant across all tasks at 8 Pa, while the pressures at the other four inlets were adjusted task-specifically to 2, 3, 4, and 6 Pa. Correspondingly, the targets for the output node's volume were set at 2, 3, 4, and 15 cc^3 for each input pressure. An epoch in this context was structured around four learning iterations, with the network undergoing simultaneous training across all tasks. The modification in resistances required for accomplishing each task was computed, and the adjustment implemented in each epoch represented the average of these calculated modifications. The simulation evidenced convergence after 500 epochs.

3. Discussion and Concluding Remarks

In this work, we combined multistability with the concept of physical neural networks and studied the properties of such physical systems. This illustrates a paradigm where mechanical

systems mimic the versatile, task-specific functionality characteristic of digital neural networks in the realm of artificial intelligence. The discussion below summarizes the current work and presents the broader implications of our findings.

Our focus was on bistable flow networks. Flow networks are characterized by internal, external, and output nodes, facilitated by either constant pressures or volumetric flow rates. The bistable nature of each network element, presenting a nonlinear pressure–volume relationship and two distinct states of positive stiffness ("0" and "1"), enables the versatility and adaptability of this system. We examined the network's potential equilibrium configurations or steady-states, analyzed their stability, and harnessed the complex dynamic behavior of the system.

The analysis of the network's steady-states and the stability of its states highlights that, in scenarios devoid of external flux or prescribed pressure, the network will reach a state of pressure equilibrium regardless of its topological configuration. Conversely, when external pressures are introduced, the resultant steady-state pressures are determined by the interplay between the network's topology and the resistances within its connecting tubes. Although the existence of steady-state configurations may be contingent upon these parameters, the stability of the network at a steady-state was found to be invariant with respect to both topology and resistance values. This insight underscores the robustness of such networks against structural and operational variabilities.

Even though one might assume that a particular configuration of the network might achieve a desired equilibrium or

**ADVANCED
SCIENCE NEWS**

www.advancedsciencenews.com

**ADVANCED
INTELLIGENT
SYSTEMS**
Open Access

www.advintellsyst.com

steady-state, complexity increases as the number of tubes exceeds the number of nodes. This gap renders the transformation indeterminate, lacking a single-valued definition. Consequently, it remains unclear whether a consistent and desirable transformation can always be established between a set of constraints and steady-states. This uncertainty highlights the complicated relationship between network architecture and its operational dynamics.

Having studied the equilibrium dynamics and stability of such networks, we investigated their complex dynamics under the control of inlet volumetric flux, which was specified for a limited duration, and revealed the network's ability to adopt distinct binary states that are influenced by its topological structure. This stage emphasized the challenge of identifying a configuration of network topologies and resistances to guide the system toward a desired equilibrium state. A global supervised learning algorithm was used to address this challenge.

The obtained outcomes showcase a pioneering concept that can be leveraged in soft robotics actuation and microfluidics applications, particularly in scenarios involving pressurized flow within cavities embedded in elastic bodies. The conventional approach to achieving complex deformation patterns involves the intricate control of multiple inputs, adding complexity to the system's operation.[33,43,64–71] Thus, significant interest exists in simplifying the control of such systems.[72–77] In our work, we introduce a novel result demonstrating single-input control over a lattice composed of bistable elastic chambers. Innovative soft actuator technology holds considerable promise for the development of soft actuators with streamlined and efficient control mechanisms.[32,34,36,64,78]

Next, we applied a local supervised learning method. This training strategy, drawing upon the mechanical attributes of the network's elements, enables the network to progress toward defined operational objectives. This part of our study reveals the potential of these networks to perform an array of tasks—such as interpolations, regressions, sorting, and classification—using purely mechanical networks.

Further, this research highlights the network's ability to function as a memory storage system. Each bistable node within the network operates as an independent data storage unit. Consequently, every stable equilibrium configuration effectively acts as a "stored memory", allowing the network to maintain the last reached state, even when disconnected from any external inputs. This characteristic facilitates the pre-setting of the network to diverse equilibrium states under uniform inputs by pre-encoding memories. This capability not only enhances the adaptability of the network but also broadens its applicability across various computational scenarios. We demonstrated how the network can write data to a memory storage. By utilizing this property, bistable PNNs have the potential to perform computations that involve storing information as memory and using it in subsequent computations.

While fabricating a physical demonstrator is beyond the scope of this work, our sensitivity analysis of the network's response to defects reveals that the training algorithms continue to succeed even with up to 20% randomized variability in bistable characteristics, despite relying on an algorithm that assumes perfectly identical node properties.

Our research yielded significant results but also faced several limitations. Physical limitations on resistance values—preventing them from being negative or approaching zero—imposed constraints that sometimes restricted convergence. Another challenge arose from the non-convex optimization model (10), as the pressure–volume bistability introduced nonlinearities, causing discontinuities in the loss and error functions. This made it difficult to rely on convergence diagrams to predict model performance. The global learning approach is limited in driving autonomous adaptation within a physical network for two primary reasons. First, adjusting each tube's conductance explicitly depends on the flux through all other tubes, regardless of their distance, requiring a network-wide scope. Second, the loss function is directly tied to the desired response, meaning that if the network were to compute the gradient, it would need to encode information about that target response. These constraints reveal that this approach requires intervention by an external designer and cannot be classified as a truly autonomous, physical learning process. Further, in testing with a 5×5 node lattice network (Figure 3), we chose to enable full connectivity among all nodes, deviating from the typical layered structure of classical neural networks. Our strategy of connecting each node to every other node in the network was observed to provide greater flexibility and a more dynamic representation of the data during training. By using this approach, the model is able to capture more complex relationships and interactions between the nodes. Future research may explore alternative connection strategies. We noted that attempts to enforce traditional layered connectivity led to model convergence issues. Based on our numerical investigations, training both smaller and larger networks was successful. However, a thorough investigation into the sensitivity of network performance to variations in the number of nodes and tubes is left for future research. In later stages, where networks were trained for specific pressure targets using a local supervised learning approach, disordered networks (without structured patterns) outperformed ordered ones, and networks with 5–6 node connections achieved better training outcomes than those with fewer or more connections, suggesting an optimal connectivity range.

Although some limitations were discovered, our work has the potential to drive important innovations in smart technologies, soft actuations, bistable structures, and other areas. Furthermore, our research lays foundational stones toward the realization of computational matter, marking the advent of learning matter. The findings of this study mark an important milestone, signaling new opportunities for future investigation.

Supporting Information

Supporting Information is available from the Wiley Online Library or from the author.

Acknowledgements

Conflict of Interest

The authors declare no conflict of interest.

Author Contributions

Ben-Haim Eran: conceptualization (lead); data curation (equal); formal analysis (lead); investigation (lead); methodology (lead); validation (lead); visualization (lead); writing—original draft (lead); writing—review & editing (equal). **Givli Sefi**: methodology (equal); visualization (supporting); writing—review & editing (supporting). **Or Yizhar**: supervision (equal); visualization (supporting); writing—review & editing (supporting). **Gat D. Amir**: conceptualization (lead); formal analysis (equal); investigation (equal); methodology (equal); supervision (lead); writing—original draft (equal); writing—review & editing (equal).

Data Availability Statement

The data that support the findings of this study are available in the Supporting Information of this article.

[1] H. C. Lai, L. Y. Jan, *Nat. Rev. Neurosci.* **2006**, *7*, 548.
[2] E. Bullmore, O. Sporns, *Nat. Rev. Neurosci.* **2012**, *13*, 336.
[3] G. W. Burr, R. M. Shelby, A. Sebastian, S. Kim, S. Kim, S. Sidler, K. Virwani, M. Ishii, P. Narayanan, A. Fumarola, L. L. Sanches, I. Boybat, M. Le Gallo, K. Moon, J. Woo, H. Hwang, Y. Leblebici, *Adv. Phys. X* **2017**, *2*, 89.
[4] D. Marković, A. Mizrahi, D. Querlioz, J. Grollier, *Nat. Rev. Phys.* **2020**, *2*, 499.
[5] Q. Duan, Z. Jing, X. Zou, Y. Wang, K. Yang, T. Zhang, S. Wu, R. Huang, Y. Yang, *Nat. Commun.* **2020**, *11*, 3399.
[6] Z. Wang, H. Wu, G. W. Burr, C. Seong Hwang, K. L. Wang, Q. Xia, J. Joshua Yang, *Nat. Rev. Mater.* **2020**, *5*, 173.
[7] D. Kuzum, S. Yu, H. S. Philip Wong, *Nanotechnology* **2013**, *24*, 382001.
[8] G. Indiveri, B. Linares-Barranco, T. J. Hamilton, A. Van Schaik, R. Etienne-Cummings, T. Delbruck, S.-C. Liu, P. Dudek, P. Häfliger, S. Renaud, J. Schemmel, G. Cauwenberghs, J. Arthur, K. Hynna, F. Folowosele, S. Saighi, T. Serrano-Gotarredona, J. Wijekoon, Y. Wang, K. Boahen, *Front. Neurosci.* **2011**, *5*, 9202.
[9] C. Bartolozzi, G. Indiveri, *Neural Comput.* **2007**, *19*, 2581.
[10] K. Roy, A. Jaiswal, P. Panda, *Nature* **2019**, *575*, 607.
[11] S. Furber, *J. Neural Eng.* **2016**, *13*, 051001.
[12] J. Kendall, R. Pantone, K. Manickavasagam, Y. Bengio, B. Scellier, *arXiv preprint arXiv:2006.01981* **2020**.
[13] M. Stern, A. Murugan, *Annu. Rev. Condens. Matter Phys.* **2023**, *14*, 417.
[14] N. Pashine, D. Hexner, A. J. Liu, S. R. Nagel, *Sci. Adv.* **2019**, *5*, eaax4215.
[15] N. Pashine, *Phys. Rev. Mater.* **2021**, *5*, 065607.
[16] B. Scellier, *arXiv preprint arXiv:2103.09985* **2021**.
[17] M. Stern, D. Hexner, J. W. Rocks, A. J. Liu, *Phys. Rev. X* **2021**, *11*, 021045.
[18] C. P. Goodrich, A. J. Liu, S. R. Nagel, *Phys. Rev. Lett.* **2015**, *114*, 225501.
[19] J. W. Rocks, N. Pashine, I. Bischofberger, C. P. Goodrich, A. J. Liu, S. R. Nagel, *Proc. Natl. Acad. Sci.* **2017**, *114*, 2520.
[20] M. Stern, V. Jayaram, A. Murugan, *Nat. Commun.* **2018**, *9*, 4303.
[21] J. W. Rocks, H. Ronellenfitsch, A. J. Liu, S. R. Nagel, E. Katifori, *Proc. Natl. Acad. Sci.* **2019**, *116*, 2506.
[22] M. Ruiz-Garca, A. J. Liu, E. Katifori, *Phys. Rev. E* **2019**, *100*, 052608.
[23] D. Hexner, A. J. Liu, S. R. Nagel, *Proc. Natl. Acad. Sci.* **2020**, *117*, 31690.
[24] M. Stern, M. B. Pinson, A. Murugan, *Phys. Rev. X* **2020**, *10*, 031044.
[25] R. H. Lee, E. A. B. Mulder, J. B. Hopkins, *Sci. Robot.* **2022**, *7*, eabq7278.
[26] V. R. Anisetti, B. Scellier, J. M. Schwarz, *Phys. Rev. Res.* **2023**, *5*, 023024.
[27] S. Dillavou, M. Stern, A. J. Liu, D. J. Durian, *Phys. Rev. Appl.* **2022**, *18*, 014040.
[28] R. G. Crowder, *Principles of Learning and Memory: Classic Edition*, Psychology Press, Hove, UK **2014**.
[29] J. R. Anderson, *Learning and Memory: An Integrated Approach*, John Wiley & Sons Inc, Hoboken, NJ **2000**.
[30] Y. Chi, Y. Li, Y. Zhao, Y. Hong, Y. Tang, J. Yin, *Adv. Mater.* **2022**, *34*, 2110384.
[31] R. A. M. Receveur, C. R. Marxer, R. Woering, V. C. M. H. Larik, N.-F. de Rooij, *J. Microelectromech. Syst.* **2005**, *14*, 1089.
[32] B. Gorissen, E. Milana, A. Baeyens, E. Broeders, J. Christiaens, K. Collin, D. Reynaerts, M. De Volder, *Adv. Mater.* **2019**, *31*, 1804598.
[33] B. Gorissen, D. Melancon, N. Vasios, M. Torbati, K. Bertoldi, *Sci. Robot.* **2020**, *5*, eabb1967.
[34] E. Ben-Haim, L. Salem, Y. Or, A. D. Gat, *Soft Robot.* **2020**, *7*, 259.
[35] Y. Cao, M. Derakhshani, Y. Fang, G. Huang, C. Cao, *Adv. Funct. Mater.* **2021**, *31*, 2106231.
[36] D. Melancon, A. E. Forte, L. M. Kamp, B. Gorissen, K. Bertoldi, *Adv. Funct. Mater.* **2022**, *32*, 2201891.
[37] E. Ben-Haim, D. Ilssar, Y. Or, A. D. Gat, *J. Fluid Mech.* **2022**, *937*, A18.
[38] M. F. Beatty, *Appl. Mech. Rev.* **1987**, *40*, 1699.
[39] J. Pfitzner, *Anaesthesia* **1976**, *31*, 273.
[40] F. Bullo, *Lectures on Network Systems*, Vol. *1*, Kindle Direct Publishing Seattle, DC, USA **2020**.
[41] H. Alexander, *Int. J. Eng. Sci.* **1971**, *9*, 151.
[42] I. Müller, P. Strehlow, *Rubber and Rubber Balloons: Paradigms of Thermodynamics*, Vol. *637*, Springer Science & Business Media, Berlin **2004**.
[43] J. T. B. Overvelde, T. Kloek, J. J. A. D'haen, K. Bertoldi, *Proc. Natl. Acad. Sci.* **2015**, *112*, 10863.
[44] H. Dal, A. K. Açan, C. Durcan, M. Hossain, *Arch. Comput. Methods Eng.* **2023**, *30*, 4601.
[45] G. Salinas, S. Givli, *Microsyst. Technol.* **2015**, *21*, 943.
[46] M. Vangbo, *Sens. Actuators, A* **1998**, *69*, 212.
[47] J. Zhao, J. Jia, X. He, H. Wang, *J. Appl. Mech.* **2008**, *75*, 041020.
[48] R. V. Mises, *ZAMM-J. Appl. Math. Mech./Zeitschrift für Angewandte Mathematik und Mechanik* **1923**, *3*, 406.
[49] G. Arena, R. M. J. Groh, R. Brinkmeyer, R. Theunissen, P. M. Weaver, A. Pirrera, *Proc. R. Soc. A* **2017**, *473*, 20170334.
[50] S. P. Timoshenko, J. M. Gere, *Theory of Elastic Stability*, Courier Corporation, Chelmsford, MA **2009**.
[51] G. W. Brodland, H. Cohen, *Int. J. Solids Struct.* **1987**, *23*, 1341.
[52] J. A. Faber, J. P. Udani, K. S. Riley, A. R. Studart, A. F. Arrieta, *Adv. Sci.* **2020**, *7*, 2001955.
[53] M. Liu, L. Domino, I. D. de Dinechin, M. Taffetani, D. Vella, *J. Mech. Phys. Solids* **2023**, *170*, 105116.

[54] L. Shui, K. Ni, Z. Wang, *ACS Appl. Mater. Interfaces* **2022**, *14*, 43802.

[55] C. D. Meyer, I. Stewart, *Matrix Analysis and Applied Linear Algebra*, SIAM, New Delhi **2023**.

[56] G. Puglisi, L. Truskinovsky, *J. Mech. Phys. Solids* **2000**, *48*, 1.

[57] P. Jain, A. Tewari, P. Kar, *Adv. Neural Inf. Process. Syst.* **2014**, *27*.

[58] R. W. Ogden, *Proc. R. Soc. Lond. A: Math. Phys. Sci.* **1972**, *326*, 565.

[59] S. Marbach, N. Ziethen, L. Bastin, F. K. Bäuerle, K. Alim, *bioRxiv* **2021**.

[60] M. Kramar, K. Alim, *Proc. Natl. Acad. Sci.* **2021**, *118*, e2007815118.

[61] A. Tero, S. Takagi, T. Saigusa, K. Ito, D. P. Bebber, M. D. Fricker, K. Yumiki, R. Kobayashi, T. Nakagaki, *Science* **2010**, *327*, 439.

[62] E. Katifori, G. J. Szöllösi, M. O. Magnasco, *Phys. Rev. Lett.* **2010**, *104*, 048704.

[63] H. Ronellenfitsch, E. Katifori, *Phys. Rev. Lett.* **2016**, *117*, 138301.

[64] K. Che, C. Yuan, H. Jerry Qi, J. Meaud, *Soft Matter* **2018**, *14*, 2492.

[65] Y. Tang, Y. Chi, J. Sun, T.-H. Huang, O. H. Maghsoudi, A. Spence, J. Zhao, H. Su, J. Yin, *Sci. Adv.* **2020**, *6*, eaaz6912.

[66] Z. Wang, X. Zhang, Y. Wang, Z. Fang, H. Jiang, Q. Yang, X. Zhu, M. Liu, X. Fan, J. Kong, *Adv. Sci.* **2023**, *10*, 2206662.

[67] P. Kaarthik, F. L. Sanchez, J. Avtges, R. L. Truby, *Soft Matter* **2022**, *18*, 8229.

[68] A. Zolfagharian, A. Kaynak, A. Kouzani, *Mater. Des.* **2020**, *188*, 108411.

[69] W. Ma, Z. Zhang, H. Zhang, Y. Li, H. Wu, S. Jiang, G. Chai, *Smart Mater. Struct.* **2019**, *28*, 025028.

[70] Y. Wu, R. Chaunsali, H. Yasuda, K. Yu, J. Yang, *Sci. Rep.* **2018**, *8*, 112.

[71] J. Kaufmann, P. Bhovad, S. Li, *Soft Robot.* **2022**, *9*, 212.

[72] P. Polygerinos, N. Correll, S. A. Morin, B. Mosadegh, C. D. Onal, K. Petersen, M. Cianchetti, M. T. Tolley, R. F. Shepherd, *Adv. Eng. Mater.* **2017**, *19*, 1700016.

[73] A. D. Marchese, R. K. Katzschmann, D. Rus, *Soft Robot.* **2015**, *2*, 7.

[74] M. A. Unger, H.-P. Chou, T. Thorsen, A. Scherer, S. R. Quake, *Science* **2000**, *288*, 113.

[75] T. Thorsen, S. J. Maerkl, S. R. Quake, *Science* **2002**, *298*, 580.

[76] A. V. Desai, J. D. Tice, C. A. Apblett, P. J. A. Kenis, *Lab Chip* **2012**, *12*, 1078.

[77] B. Mosadegh, C.-H. Kuo, Y.-C. Tung, Y. Torisawa, T. Bersano-Begey, H. Tavana, S. Takayama, *Nat. Phys.* **2010**, *6*, 433.

[78] L. S. Novelino, Q. Ze, S. Wu, G. H. Paulino, R. Zhao, *Proc. Natl. Acad. Sci.* **2020**, *117*, 24096.